

Micropyramid structured photo capacitive interfaces

Nikić, Marta; Opančar, Aleksandar; Hartmann, Florian; Migliaccio, Ludovico; Jakešová, Marie; Głowacki, Eric Daniel; Đerek, Vedran

Source / Izvornik: **Nanotechnology, 2022, 33**

Journal article, Published version

Rad u časopisu, Objavljena verzija rada (izdavačev PDF)

<https://doi.org/10.1088/1361-6528/ac5927>

Permanent link / Trajna poveznica: <https://um.nsk.hr/um:nbn:hr:217:066532>

Rights / Prava: [Attribution 4.0 International](#)/[Imenovanje 4.0 međunarodna](#)

Download date / Datum preuzimanja: **2024-12-01**






Repository / Repozitorij:

[Repository of the Faculty of Science - University of Zagreb](#)



Micropyramid structured photo capacitive interfaces

Marta Nikić¹, Aleksandar Opančar¹, Florian Hartmann^{2,3} ,
Ludovico Migliaccio⁴, Marie Jakešová⁴, Eric Daniel Głowacki^{4,*}  and
Vedran Đerek^{1,*} 

¹ Department of Physics, Faculty of Science, University of Zagreb, Bijenička c. 32, 10000, Zagreb, Croatia

² Soft Matter Physics, Institute of Experimental Physics, Johannes Kepler University Linz, Altenberger Strasse 69, Linz, A-4040, Austria

³ Soft Materials Lab, Linz Institute of Technology LIT, Johannes Kepler University, Altenberger Strasse 69, Linz, A-4040, Austria

⁴ Central European Institute of Technology, Brno University of Technology, Purkyňova 123, 61200 Brno, Czech Republic

E-mail: eric.daniel.glowacki@ceitec.vutbr.cz and vdjerek@phy.hr

Received 12 November 2021, revised 1 February 2022

Accepted for publication 28 February 2022

Published 23 March 2022



Abstract

Optically driven electronic neuromodulation devices are a novel tool in basic research and offer new prospects in medical therapeutic applications. Optimal operation of such devices requires efficient light capture and charge generation, effective electrical communication across the device's bioelectronic interface, conformal adhesion to the target tissue, and mechanical stability of the device during the lifetime of the implant—all of which can be tuned by spatial structuring of the device. We demonstrate a 3D structured opto-bioelectronic device—an organic electrolytic photocapacitor spatially designed by depositing the active device layers on an inverted micropyramid-shaped substrate. Ultrathin, transparent, and flexible micropyramid-shaped foil was fabricated by chemical vapour deposition of parylene C on silicon moulds containing arrays of inverted micropyramids, followed by a peel-off procedure. The capacitive current delivered by the devices showed a strong dependency on the underlying spatial structure. The device performance was evaluated by numerical modelling. We propose that the developed numerical model can be used as a basis for the design of future functional 3D design of opto-bioelectronic devices and electrodes.

Supplementary material for this article is available [online](#)

Keywords: bioelectronics, micropyramids, photocapacitors, neurostimulation


(Some figures may appear in colour only in the online journal)

1. Introduction

Wireless neuromodulation has been a widely researched topic [1–4] resulting in different practical approaches such as

battery-powered [5, 6] and remotely operated [7, 8] devices, as well as remotely powered and controlled devices. Implants can be remotely powered by ultrasound [7, 9], magnetic induction [2, 10], radiofrequency electromagnetic waves [11–13], as well as driven by light [14–17]. Intrinsically remotely controllable neuromodulation methods have been developed, such as optical thermo-capacitive neurostimulation [18–20] and optogenetics [21–23]. All of the aforementioned methods have the advantage for *in vivo* experimental and therapeutic usage in comparison to wired devices. However, most of them are attached to a set of limitations and

* Author to whom any correspondence should be addressed.

 Original content from this work may be used under the terms of the [Creative Commons Attribution 4.0 licence](#). Any further distribution of this work must maintain attribution to the author(s) and the title of the work, journal citation and DOI.

disadvantages, such as a large form factor [24], limited tissue penetration [25] and the need for complex external apparatus for powering and controlling the implants [26]. Implants offering effective and stable operation, minimally invasive form-factor and simple remote power and control would have a distinct advantage over the competing technologies. Moreover, tunability of the device operation when being to a specific usage scenario is desirable.

Organic electrolytic photocapacitors (OEPCs), thin-film based devices for extracellular electric neurostimulation have been used in single-cell models [27], *in vitro* in explanted retina and neuronal cell cultures [28], as well as *in vivo* in animal models, in both acute and chronic examples [29]. The OEPC devices showed effective, reproducible and stable performance for over 100 d in chronic *in vivo* experiments. The devices consist of an optically transparent substrate acting as mechanical support, covered by a conductive and transparent back electrode, on which an active *pn* organic semiconductor bilayer thin film is grown and patterned by physical vapour deposition (PVD). The substrate of choice for planar devices used in chronic peripheral nerve implantation was ultrathin ($<10\ \mu\text{m}$) flexible parylene C foil, topped with a transparent conductive thin film of gold. Recently, a fabrication method of spatially structured parylene C foils for applications in stretchable electronics was demonstrated, using parylene C chemical vapour deposition (CVD) on silicon microgroove moulds, followed by a peel-off process [30]. A similar method, based on parylene C CVD on silicon micropillar moulds, followed by a structured parylene film transfer was used in this work for the fabrication of parylene C micropillar arrays.

Thin films of small-molecule organic pigments metal-free phthalocyanine (H_2Pc) and a perylene derivative $\text{N,N}'$ -dimethyl perylenetetracarboxylic diimide (PTCDI) were used as optically active p and n-type semiconducting layers. Hydrogen bonded organic pigments were shown to be stable in devices operating in aqueous conditions [31], thus the top n-type PTCDI layer was in direct contact with the excitable cells and/or living tissue. All the constituent materials used in OEPC devices, namely parylene C, gold and H_2Pc and PTCDI have well established biocompatibility record [29]. The parylene C planar devices' thin and flexible form factor had enabled conformal wrapping of the device around the peripheral nerve. However, the geometry's inherent limitations, such as low friction between the device and the tissue, non-elasticity and highly directionally dependent light absorption were noted. Therefore, to address some of the limitations of the planar geometry, the OEPC devices were used as model devices and were fabricated on 3D micropillar structured parylene C foils to demonstrate the effects of spatial structuring of thin-film opto-bioelectronic interfaces. The spatially structured devices have inherited the intrinsic flexibility of the parylene C substrate (figure 1), as well as a level of elasticity afforded by the folded parylene C geometry. The improved mechanical traits of the device may be of use for future bioelectronic applications.

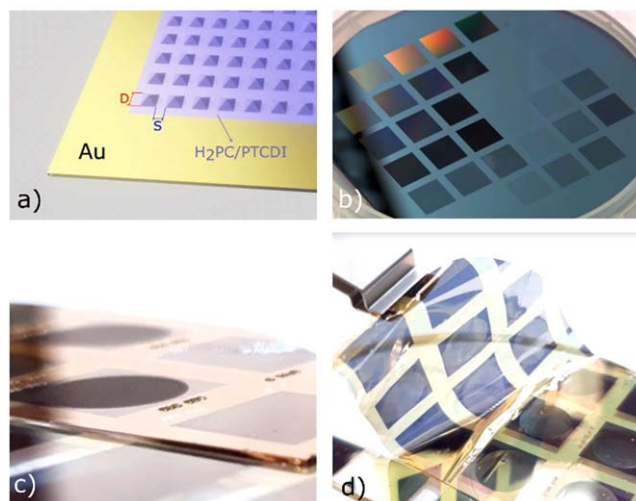


Figure 1. (a) Illustration of a finished self-standing device with array of micropillars of base size D and spacing S and (b) a finished silicon mould with arrays of etched inverted micropillars; (c) a cross-section photograph of the finished devices on a glass wafer and a PDMS backing layer and (d) peeling off a micropillar structured parylene C foil with OEPC devices from the PDMS backing layer.

2. Experimental methods

2.1. Mould fabrication

A 10 cm diameter (100) crystallographically oriented silicon wafer was used to fabricate the mould for microstructuring the parylene C substrate for the OEPC devices (figure 2). A 140 nm thick silicon nitride (SiN) layer was deposited by plasma-enhanced chemical vapour deposition (PECVD) on both sides of the silicon wafer and used as an etch mask layer for anisotropic wet etching of silicon. Square openings designating the micropillar patterned areas were defined by photolithography. Adhesion promoter hexamethyl disilazane (HMDS) was vapour-phase deposited on the bake-dried SiN surface. Wafers were rinsed with acetone, isopropanol, and deionized water, and finally thoroughly rinsed and dried using an acetone-DI water spin dryer. Patterning of SiN was done using Dow S1818 G2 (S1818) photoresist. S1818 was spin-cast by ramping from 500 rpm to 4000 rpm for 5 s and continuing at 4000 rpm for 30 s, followed by a soft-bake at $90\ ^\circ\text{C}$ for 90 s, typically giving a photoresist thickness of $2\ \mu\text{m}$. A chromium glass photomask was designed and used for defining the micropillar arrays. Each array consisted of 10 mm by 10 mm area, patterned with square openings of base size D ($D = 2, 4, 6, 18$ and $54\ \mu\text{m}$) and spacing S ($S = 2, 3, 4, 6, 18$ and $54\ \mu\text{m}$), giving a total of 30 arrays with different combinations of pillar base size and spacing per one silicon wafer mould.

The photoresist was exposed by a Karl Süss MA6/BA6 mask aligner using a 350 W mercury vapour lamp calibrated to the power of $15\ \text{mW cm}^{-2}$ at a wavelength of 405 nm for 4 s using a high vacuum mode. The photoresist was developed using the Microposit MF-319 developer. Post-exposure bake was done at $110\ ^\circ\text{C}$ for 60 s. The exposed areas of SiN were removed by CF_4/O_2 reactive ion etching (RIE) under the

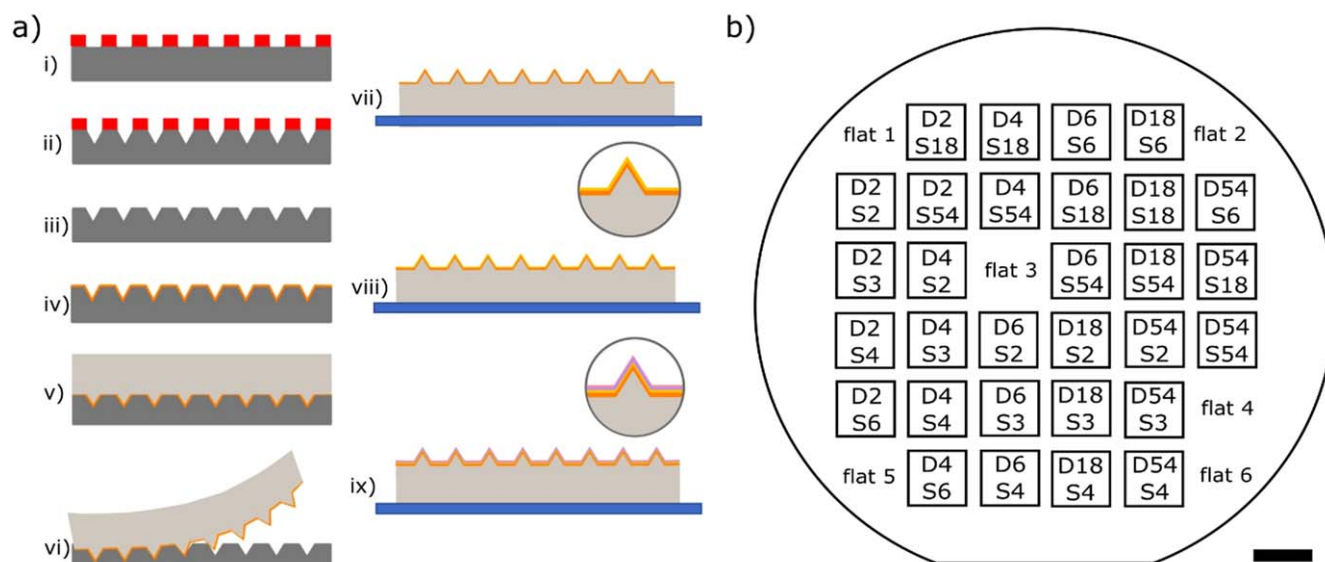


Figure 2. (a) Fabrication steps of the OEPC device on top of structured flexible parylene C substrates: (i) SiN hard mask deposition on (100) Si wafer, (ii) anisotropic etching of silicon, (iii) silicon mould after the removal of the hard mask, (iv) deposition of anti-adhesion treatment, followed by parylene C via CVD on a silicon mould, (v) drop casting of PDMS elastomer mechanical support layer, (vi) peel-off of the PDMS and structured parylene C, (vii) flipping and transfer of the sample to a transparent glass wafer, (viii) deposition of a thin Au layer, and (ix) deposition of active organic semiconductor layers. (b) Layout of micropylramid arrays with base length D and spacing S on a test device, with indicated flat reference measurement areas. An outline of a 100 mm (100) oriented silicon wafer is shown in red. Scale bar is 10 mm.

working pressure of 100 mbar, with gas flows of 500 sccm and 25 sccm respectively. Plasma was excited by a 50 W RF source. Photoresist stripper 1112A (MicroChem) heated to 60 °C was used for stripping of the remaining photoresist. Wafers were oxygen plasma de-scummed using a plasma cleaner (Diener electronic GmbH + Co. KG) for 10 min using plasma excited by a 200 W RF source.

Prior to the anisotropic etching of the silicon, a thin layer of SiO₂ created during the plasma cleaning process had to be removed for improved Si etching uniformity. Buffered oxide etch, BOE 7:1 (Microchemicals) etching solution was used at room temperature for 5 s followed by a DI water rinse cycle. Anisotropic etching of the silicon was performed in a reflux condenser-covered container, in a 30% wt potassium hydroxide (KOH) aqueous solution saturated with 2-propanol at 80 °C, with the solution being mixed with a magnetic mixer at 800 rpm, using a setup described in [32]. Time of etching depended on the desired microstructured pyramid size for the mould [33]. Etched wafers were thoroughly rinsed with DI water. The remaining SiN passivation layer was removed using a BOE etching solution at room temperature for 2 min, followed by a DI water rinse.

To facilitate the parylene C peel off, an anti-adhesion layer had to be deposited on the finished mould by vapour phase silanization. Before the silanization, the hydrogen-terminated Si mould surface was oxygen plasma treated to create the anchoring points for the silanization process, using an oxygen plasma cleaner (Diener), with 100 W RF plasma excitation for 10 min. Silanization was conducted using a neat 100 µl aliquot of trichloro (1H, 1H, 2H, 2H-perfluorooctyl) silane (FOTS) in a closed container for 2 h at room temperature. Silanized moulds were then sonicated in acetone,

2-propanol and DI water for 15 min each to remove possible FOTS multilayers.

2.2. Structured parylene C substrate fabrication

Parylene C film of 2 µm thickness was deposited on the silanized moulds using a parylene C deposition system (Diener electronic GmbH + Co. KG) with 10 g of granular parylene-C dimer (TiXX Coatings GmbH). The dimer was vaporized at a temperature of 170 °C at a system pressure of 10⁻² mbar and then pyrolyzed at 650 °C in the pyrolyzing tube furnace. The deposition was carried out at room temperature, with wafers placed on a rotating carousel in the deposition chamber. Oxygen plasma activation of the deposited parylene C surface was conducted using a plasma cleaner at 50 W RF plasma excitation for 3 min. The mould with the conformally deposited parylene C film was placed in a plastic petri dish, and a 2–3 mm thick layer of SYLGARD 184 polydimethylsiloxane (PDMS) with a 10:1 ratio of base versus curing agent was cast on top of the parylene C covered mould surface and cured at 40 °C overnight. Low curing temperatures are required to prevent the formation of wrinkles after the peel off. A surgical scalpel was used to manually circumscribe the PDMS and parylene C layers from the edges of the silicon mould. The obtained PDMS/parylene C film was carefully separated from the mould and, with the PDMS side facing downwards, transferred to a clean glass wafer, with the micropylramid arrays being faithfully reproduced in the thin parylene C film, with the PDMS layer acting as mechanical support for the parylene C film.

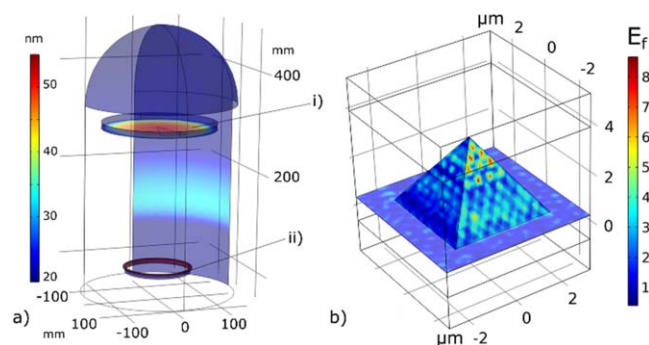


Figure 3. COMSOL Multiphysics finite element model of (a) deposited film thickness inside a thermal evaporator, using the Molecular Flow module with (i) sample stage containing the micropillar structured substrate and (ii) circular evaporation source, mimicking sample stage rotation; and (b) light trapping, using the parametric study by the Wave Optics module, for a $D = 4$ and $S = 2$ unit cell. E_f shows the light enhancement factor over the planar substrate.

2.3. OEPC device fabrication

Before deposition of a transparent gold layer, the parylene C surface was oxygen plasma activated using a plasma cleaner under a 50 W RF excitation for 3 min. Gold was deposited in a thermal PVD system pumped down to 2×10^{-6} mbar at a rate of $1.5\text{--}2.5 \text{ \AA s}^{-1}$ to a thickness of 20 nm. After the deposition of gold, strips between the micropillar arrays were masked using PVC adhesive tape. Deposition of the organic semiconductors was done with a multisource organic thermal PVD system (Moorfield/Edwards 306A) pumped down to 1×10^{-6} mbar. H_2Pc was evaporated at a rate of $1\text{--}2 \text{ \AA s}^{-1}$ to a thickness of 50 nm, and PTCDI was evaporated at a rate of $1.5\text{--}2.5 \text{ \AA s}^{-1}$ to a thickness of 50 nm. Both materials were purified three times by temperature gradient sublimation.

2.4. Measurements

OEPC device performance was evaluated by measuring photocurrent traces after the square light pulse excitation (100 ms on, 5000 ms off) from below the device (figure 7). Light excitation was achieved with a 630 nm 3 W LED placed behind a transparent glass window below the sample stage, giving an irradiance of 60 mW cm^{-2} at the sample position on the stage. At 630 nm mainly the H_2Pc material is absorbing light and generating charges, while PTCDI is optoelectronically mostly passive—thus, H_2Pc is the dominantly absorbing layer (SI 1 (available online at stacks.iop.org/NANO/33/245302/mmedia)) [28]. Contact to the gold back electrode of the devices was established with a needle probe, while the electrolyte contact was achieved with an Ag/AgCl electrode immersed in 0.1 M KCl electrolyte in a 1 ml syringe placed on an xyz-stage above the sample. Using an empty syringe connected by flexible tubing to the electrode-containing syringe, the level of the electrolyte in the electrode-containing syringe was controlled manually by adjusting the pressure. Contact with the device was established by a drop of electrolyte, without mechanical contact with the syringe. The

contact area of the drop was controlled and kept constant at $\sim 3 \text{ mm}^2$ for all measurements. At least four measurements were taken for each sample. In this work we have not conducted mechanical and opto-electronic stability studies. However, the samples have been measured repeatedly over periods of months, and the opto-electronic degradation was on par with previously reported planar devices [27, 29]. The photocurrent data was collected using a high-resolution 15 bit two-channel oscilloscope (PicoScope 5243B), connected to a low-impedance low-noise current amplifier (FEMTO DLPCA-200). All measurements were conducted inside a dark faraday cage. Scanning electron micrographs were taken using a Zeiss Sigma 500 field-emission SEM with the Inlens secondary electron detector and an acceleration voltage of 1 kV.

3. Numerical modelling

Numerical modelling was conducted using a finite-element analysis software COMSOL Multiphysics 5.6, using the Molecular Flow module for studying the effect of the geometric structuring on the thickness of films deposited by physical vapour deposition and using the Wave Optics module for a study of light trapping (figure 3). To understand how the geometrical structuring affects the device performance, geometric models of the devices with different D and S parameters were designed and used for numerical modelling of properties of interest for a given device. Micropillars were modelled as upright four-sided pyramids with base D and height of $\sqrt{2} \frac{D}{2}$, given by the symmetry properties of the silicon monocrystal. A faithful to-scale 3D model of the thermal evaporator chamber used for the thin film deposition (for both gold electrode and the organic pigment active layers) was designed, with a linear array of micropillars on a flat substrate modelled at the height of the rotating substrate holder. A circular evaporation boat was modelled by rotational extruding the evaporation crucible over a full angle, to mimic the effects of the rotation of the sample holder. The model was run in the regime of free molecular flow, where the mean free path length of evaporated material is larger than the chamber size, thus the evaporated material was deposited on the substrate following the lines of sight between the source and the substrate.

For understanding light trapping, a parametric study in the scattered field regime was designed using a micropillar with a given side dimension D and spacing $S/2$ until the edge of the elementary cell, using a Floquet periodic condition on the sides of the elementary cell. Below and above the elementary cell, swept-mesh domains of perfectly matched layers were placed. A background plane wave was emitted below the micropillar, perpendicular to its base. A thin 20 nm gold layer was modelled at the device plane, and the root mean square of the time average of the power flow 10 nm above the gold surface was monitored, signifying the light power present at the position of the device's active absorbing layer. For comparison, a planar device of the same size was

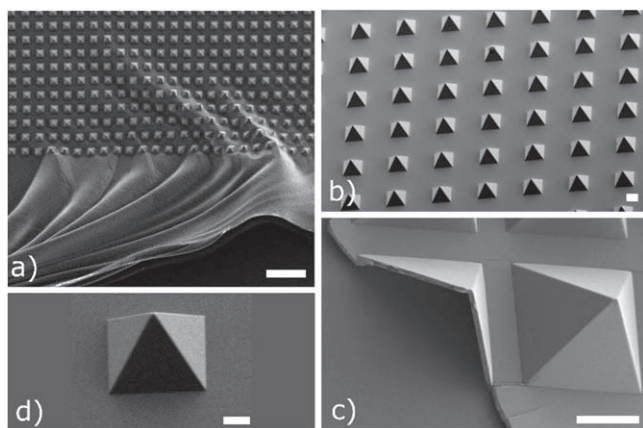


Figure 4. SEM micrographs of free-standing micropylramid structured parylene C foil. Scale bars are (a) 100 μm , (b) and (c) 10 μm and (d) 1 μm .

modelled at the same time. A ratio of integrated power flows over the structured and planar device area was taken and used in further analysis as a light-trapping enhancement factor for a given geometry.

4. Results and discussion

Chemical vapour deposition of parylene C enables conformal and uniform thickness coating of 3D surfaces [34]. Parylene C was deposited on a prepared mould, and 2 μm thick free-standing structured films were peeled off and examined by electron microscopy. Parylene C foil had faithfully reproduced the smallest features of the mould. Structured free-standing thin foils are flexible and prone to wrinkling (figure 4). Thus, parylene C thin films deposited on the mould were covered with a PDMS support layer and transferred to a glass wafer (see Methods section) for further processing steps and measurements. Glass wafer and the PDMS supporting layer enable easy handling of the sample, as well as optical transparency needed for the bottom illumination. At the end of the fabrication procedure, parylene C foil could be easily peeled off from the PDMS backing layer, liberating the free-standing device (figure 1).

4.1. PVD of the device active layers

Active layers of the OEPC—thin gold as the transparent back electrode and a pn bilayer consisting of H_2Pc and PTCDI, were deposited by thermal vacuum evaporation in the free molecular flow regime, yielding a line-of-sight non-3D conformal deposition process. To even out the contributions due to the non-central placement of the evaporation sources, the substrate holder was rotated during the deposition process. The thickness of the deposited films was controlled by a quartz crystal microbalance. In contrast to CVD methods, PVD will produce conformal films of uniform thickness only on planar substrates, while evaporation on tilted or spatially structured substrates may produce films of different thicknesses [35]. Controlling the film thickness is of critical

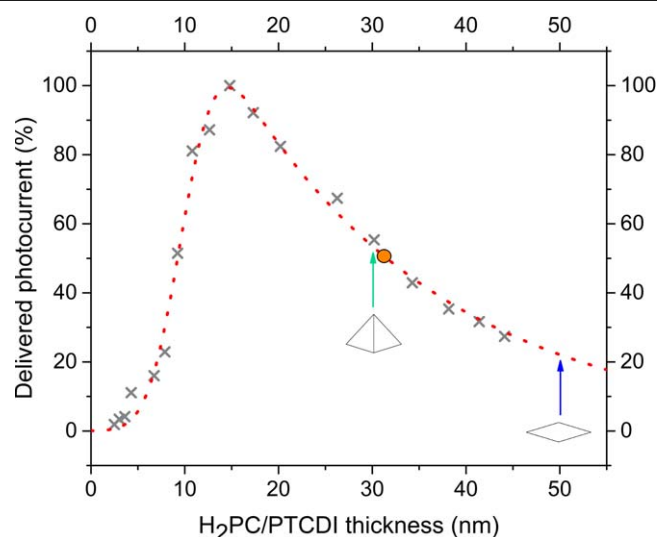


Figure 5. Relative photocurrent versus H_2Pc /PTCDI layer thickness. Gray x-marks represent measured values, red dotted line is an exponentially modified Gaussian fit curve serving as an eye-guide and for extrapolation of up to 50 nm of thickness. Blue and green arrows show the delivered current from a 50/50 nm planar and all—micropylramid structured film ($S = 0$) respectively. The orange circle represents the best performing geometry measured on a micropylramid structured film.

importance for the OEPC devices. The thickness of the bottom gold layer determines the back-electrode transparency, while the thickness of the absorbing material H_2Pc sets the maximum current the device can provide given a constant illuminance. While the optical absorbance of a gold film is a linear function of its thickness and thus can easily be taken into account, the dependence of the delivered current on the thickness of the semiconductor absorbing layer is more complicated as it involves optical absorption, charge generation and recombination. Thus, a series of planar devices with different thicknesses of pn layers in the range of 2–45 nm were fabricated. It was found that the thickness of the absorbing layer which delivers the maximal current is about 15 nm (figure 5). In thinner layers the delivered current is dominantly limited by the amount of absorbed light, since majority of the photo-generated excitons can reach the charge-separating pn interface. In thicker layers the dominant current limiting factor is the recombination of excitons close to the $\text{Au}/\text{H}_2\text{Pc}$ interface due to the short mean exciton diffusion length in H_2Pc , thus the delivered current falls off with increasing thickness [36]. Additionally, a series of planar devices with H_2Pc thickness fixed to 15 nm and varying thickness of the PTCDI in the range of 2–45 nm was fabricated. It was found that the thickness of the PTCDI does not influence the delivered current when the PTCDI thickness is above 5 nm. This shows that the thickness of the absorbing semiconductor layer is critical to the performance of the OEPC device. To elucidate thickness effects on differently structured substrates, a to-scale numerical finite element model of the PVD chamber used for evaporation of gold and organic semiconductor materials was designed, with a linear

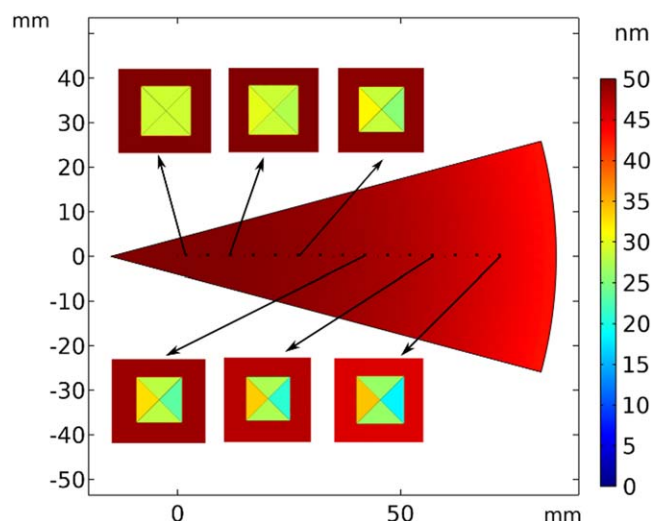


Figure 6. Results of a finite element numerical model for thickness of evaporated films on micropylamid structured substrate—top view of the slice of a sample stage with a radially ordered linear array of micropylamids.

array of micropylamids modelled radially from the centre of the sample stage.

The model's result shows a 4% decrease of thickness on the planar part of the substrate from the centre of the stage to the radial distance of 40 mm, which is the position where the most distant micropylamid array was located during the evaporation, as expected for a planar substrate and a point-like thermal evaporation source. The thickness of the evaporated layer at the sides of the micropylamid positioned at the centre of the sample stage is uniform over all of the pyramid sides due to the rotational symmetry. The thickness of the pyramid sides is reduced due to their tilt relative to the base plane, defined by the angle between the (100) and (111) crystal planes of silicon equal to $\cos^{-1}(1/\sqrt{3}) \approx 54.74^\circ$. The surface area of the pyramid sides relative to the pyramid base is larger by a factor of $\sqrt{3}$, causing the reduction of the thickness of the deposited layer at the pyramid sides to the $1/\sqrt{3}$ of the planar layer thickness next to the sides of the pyramid. Moving away from the centre of the sample stage in the radial direction, the rotational symmetry is no longer valid and the placement of the evaporation source favours the inner sides of the micropylamids, giving increased thickness there, while layer thickness at the azimuthal sides remains the same, within the limits of the radial thickness variation as observed at the planar substrate (figure 6). At the extreme radial position of interest at $r = 40$ mm, the inner micropylamid side is 17% thicker than the azimuthal sides, while the outer side is 17% thinner. This considerable difference in thickness is important to take into account when analyzing the device performance. The total current delivered from the device is a sum of the currents delivered from each pyramid side and the base plane. If the current shows linear dependence on the thickness regime between ~ 10 and 50 nm (figure 5), the contributions to the total delivered current from the device given by the respective increase and decrease of the inner and outer

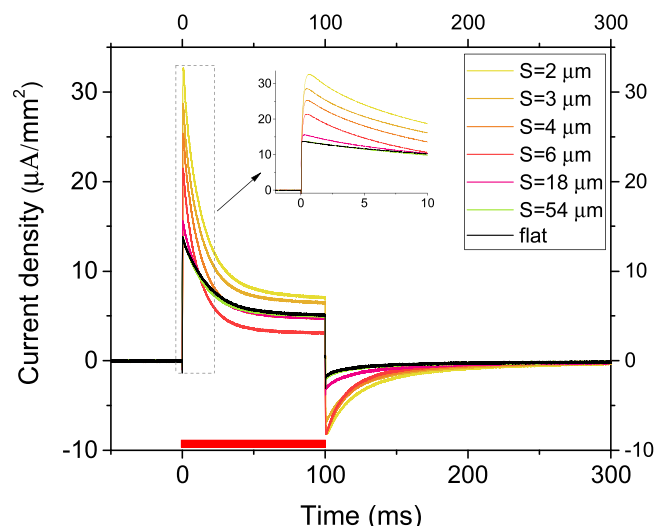


Figure 7. Current density traces of micropylamid-structured devices in comparison to a flat device, when excited with a rectangular 100 ms light pulse (red line). Traces are shown for devices with the same pyramid base size $D = 4 \mu\text{m}$ and $S = 2, 3, 4, 5, 18$ and $54 \mu\text{m}$.

pyramid sides cancel out. Thus, this variation of thickness does not have to be taken into account in further analysis. However, the average reduction of thickness by a factor of $1/\sqrt{3}$ on the sides of the pyramids leads to an increase of delivered current by a factor of approximately 2.5 for a planar layer thickness of 50 nm, under the conditions of equal light irradiation. The effective surface area of the micropylamid is larger by a factor of $\sqrt{3}$ than the area of the base of the pyramid. However, this cannot lead to an increase of the delivered current in comparison to the planar device since the delivered light is decreased by the same factor. Nevertheless, the thickness modulation factor gives a theoretical maximal increase of the delivered current by a factor of 2.5 in comparison to the planar device deposited under the same conditions, for a case where $S = 0$.

4.2. Geometric enhancement of the delivered current

The entire sample, together with the PDMS backing layer and a carrier glass, was placed at a fixed height above a LED light source. The maximum delivered current of the prepared devices on micropylamid structured parylene C foils was measured at four positions within each array. The OEPC shows a capacitive response to a rectangular light pulse, and the average value of the peak current was taken of all measurements. Response from a planar substrate was measured at four pre-defined planar locations on the sample positioned so that each structured array is adjacent to a planar control device (figure 2(b)). The thickness of the gold layer (20 nm) and the active *pn* layer (50 nm) was chosen so that the geometric thinning effects keep the device within the limits of previously reported [28] thickness values (10 nm for Au, 30/30 nm for the *pn* layer). A ratio of the delivered current of the structured device versus the neighbouring planar device is reported. Due to the limits of available photolithography tools, the minimal spacing between the pyramids

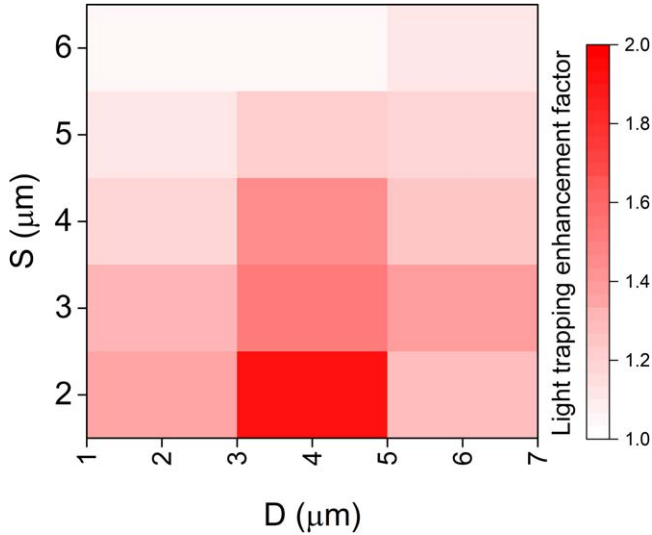


Figure 8. Light trapping enhancement factor obtained by numerical modelling for OEPC devices fabricated on micropylramid structured parylene C substrate.

was $S = 2 \mu\text{m}$, so the limiting case with $S = 0$ could not be tested. The maximum current enhancement factor due to the geometric thinning, according to the data from (figure 5) should be the largest for $S = 0$ and not larger than 2.5. The highest enhancement factor measured was 2.37.

4.3. Light trapping effects

The effects of multiple light reflections at the internal sides of the micropylramid at the interface with the active layer, as well as wave diffraction effects in the tips of the micropylramids whose dimensions are comparable to the wavelength of the light, could not be measured separately from the geometric enhancement effects. To study the light trapping, a parametric 3D numerical study of electromagnetic wave propagation at the interface of the transparent back electrode and the optically active semiconductor layer was conducted. The results show increased light absorption by up to a factor of 2 due to the light trapping for $D = 4 \mu\text{m}$ and $S = 2 \mu\text{m}$ (figure 8), and are valid for the used wavelength of 630 nm. Similar numerical analysis can be used for the rational design of other light-trapping structures for the desired wavelength.

4.4. Model of geometric performance enhancement

We propose a comprehensive model of the generated photocurrent by the micropylramid structured devices. The model separates the photocurrent enhancement into the contributions from the flat and the micropylramid-structured part of the sample and is given as a factor of the incident light power P , sample effective surface area factor A , active layer thickness-dependent current factor k , and a light-trapping current enhancement factor I_{lt} as:

$$I_f = k_{flat} P_{flat} A_{flat} + k_{pyr} I_{lt} P_{pyr} A_{pyr}. \quad (i)$$

Due to the geometry of the micropylramids, the incident light

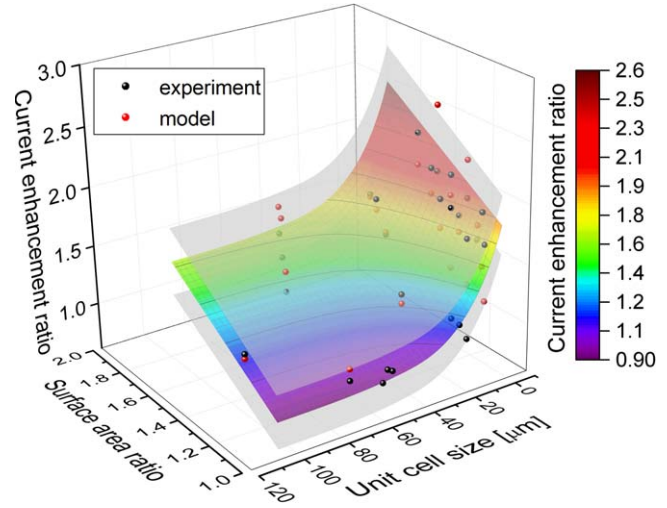


Figure 9. Measured (black) and modelled (red) current enhancement ratios. High enhancement ratios are observed and predicted for small unit cells with small spacing, giving high surface area ratios, in agreement with the model (ii).

intensity at the pyramid and the flat part is defined as:

$$P_{pyr} = \frac{1}{\sqrt{3}} P_{flat}.$$

At the same time, the effective area of the pyramid structured part of the sample is larger by a $\sqrt{3}$ factor than the area of the base of the pyramid:

$$A_{pyr} = \sqrt{3} A_{base}.$$

Thus, the $\sqrt{3}$ factor cancels out in equation (i), and the only contribution to the current enhancement comes from the enhancement by the thickness factors and the light trapping. Equation (i) can thus be given by the parameters of the unit cell $D + S$ of the micropylramid array, and the measured thickness and light trapping enhancement factors:

$$\begin{aligned} A_{base} &= D^2 \\ A_{flat} &= (D + S)^2 - A_{base}^2 = 2DS + S^2 \\ \frac{k_{pyr}}{k_{flat}} &= 2.5 = k \end{aligned}$$

Finally,

$$I_f = P_{flat} (2.5 \cdot I_{lt} \cdot D^2 + 2DS + S^2). \quad (ii)$$

The measured current enhancement factors for the geometries given by the combinations of D and S were least-squares fitted to the equation (ii), where the light trapping factors I_{lt} were taken from the numerical model, and the thickness enhancement factor k was used as a fitting parameter. The fitting procedure gave the result of $k_{fit} = (2.2 \pm 0.2)$ with the reduced chi-squared value of 0.16—as shown in (figure 9). The model predicts the largest current for small and closely packed pyramids ($D = 4 \mu\text{m}$ and $S = 2 \mu\text{m}$), which is in general agreement with the experiment, with the highest measured current for $D = 6 \mu\text{m}$ and $S = 2 \mu\text{m}$. The presented model can be used for the optimization of the delivered current given by the

micropyramid structured OEPC, given the thickness enhancement factors and light trapping enhancement factors.

5. Conclusions

A method for fabrication of optoelectronic devices on micropyramid-structured free-standing ultrathin parylene C foils was presented. Presented fabrication and optimisation methods may present significant advantages for future miniaturized high efficiency optoelectronic stimulators with improved mechanical properties and tissue adhesion. Current enhancement factors of the 3D structures in comparison to the flat devices were measured. A study was conducted of the thickness dependence of the optoelectronically active layers on the delivered current by the devices, accompanied by the numerical model of the PVD thermal evaporation process on the 3D structured substrates. Light trapping in the micropyramid structured devices was studied by a numerical wave-optics model, and light absorption enhancement by the micropyramid structures was evaluated. A comprehensive model of the delivered current depending on the geometry of the structured substrate, the thickness enhancement and the light-trapping enhancement was presented, giving reasonable agreement with the measurements. A presented model can be used for the optimization of the micropyramid structured OEPC devices but can also serve as a basis for the study of other similarly structured opto-bioelectronic devices. Using moulded micropyramid structures, we increase photo-capacitive charge density by up to 2.5 times. Charge density is a critical parameter for neurostimulation electrodes [37]. In photo-driven devices, light power to charge conversion efficiency is crucial. Our results inform how to use thickness and microstructure to influence this parameter. It is of vital importance to emphasize the need for careful consideration of the active layer thickness deposited on non-planar substrates by PVD in a free molecular flow regime. Rational use of the thickness dependant current delivery capability of the 3D structured active layers deposited by PVD processes may provide important advantages in a new generation of 3D opto-bioelectronic devices, along with the optimization of the light absorption enhancement by the light trapping effects.

Acknowledgments

This work has been supported by the Croatian Science Foundation under project UIP-2019-04-1753 (VĐ, AO, MN). We acknowledge the support of project CeNIKS, co-financed by the Croatian Government and the European Union through the European Regional Development Fund—Competitiveness and Cohesion Operational Programme (grant no. KK.01.1.1.02.0013), and the QuantiXLie Center of Excellence, a project co-financed by the Croatian Government and European Union through the European Regional Development Fund—the Competitiveness and Cohesion Operational Programme (grant no. KK.01.1.1.01.0004) (VĐ AO). Financial support by the Center of Excellence for Advanced

Materials and Sensors, Croatia, is gratefully acknowledged (VĐ). This project has received funding from the European Research Council (ERC) under the European Union's Horizon 2020 research and innovation programme (grant agreement no. 949191, E.D.G.). We acknowledge CzechNanoLab Research Infrastructure supported by MEYS CR (LM2018110).

Data availability statement

All data that support the findings of this study are included within the article (and any supplementary files).

Author contributions

VĐ and EDG conceived the research project; VĐ designed the research; MN, VĐ, AO, MJ, LM and FH did the fabrication; MN, VĐ and AO conducted the opto-electronic characterization; VĐ and MN recorded the microscopy images; VĐ performed FE analysis; VĐ and MN analyzed the data; VĐ wrote the manuscript with contributions from all authors.

ORCID iDs

Florian Hartmann  <https://orcid.org/0000-0002-5481-9850>

Eric Daniel Głowacki  <https://orcid.org/0000-0002-0280-8017>

Vedran Đerek  <https://orcid.org/0000-0001-9507-6865>

References

- [1] Katz E (ed) 2014 *Implantable Bioelectronics* 1st edn (Weinheim: Wiley-VCH)
- [2] Li X, Xiong H, Rommelfanger N, Xu X, Youn J, Slesinger P A, Hong G and Qin Z 2021 *Matter* **4** 1484–510
- [3] Won S M, Cai L, Gutruf P and Rogers J A 2021 *Nat. Biomed. Eng.* **2021** 1–19
- [4] Burton A *et al* 2021 *Microsyst. Nanoeng.* **7** 1–12
- [5] Lanmüller H, Sauermann S, Unger E, Schnetz G, Mayr W, Bijak M, Rafolt D and Girsch W 1999 *Artif. Organs* **23** 399–402
- [6] Carburanu R, Whitehurst T, Jaax K, Koff J and Makous J 2004 *26th Annu. Int. Conf. IEEE Eng. Med. Biol. Soc.* **4** 4193–6
- [7] Piech D K, Johnson B C, Shen K, Ghanbari M M, Li K Y, Neely R M, Kay J E, Carmena J M, Maharbiz M M and Muller R 2020 *Nat. Biomed. Eng.* **4** 207–22
- [8] Park J, Tabet A, Moon J, Chiang P-H, Koehler F, Sahasrabudhe A and Anikeeva P 2020 *Nano Lett.* **20** 6535–41
- [9] Seo D, Neely R M, Shen K, Singhal U, Alon E, Rabaey J M, Carmena J M and Maharbiz M M 2016 *Neuron* **91** 529–39
- [10] Chen R, Romero G, Christiansen M G, Mohr A and Anikeeva P 2015 *Science* **347** 1477–80
- [11] Gutruf P 2019 *Nat. Commun.* **10** 5742–52
- [12] Xu Q, Hu D, Duan B and He J 2015 *IEEE Trans. Neural Syst. Rehabil. Eng.* **23** 683–92

- [13] Kiani M and Ghovanloo M 2010 *IEEE Trans. Circuits Syst. II* **57** 260–4
- [14] Jiang Y, Parameswaran R, Li X, Carvalho-de-Souza J L, Gao X, Meng L, Bezanilla F, Shepherd G M G and Tian B 2019 *Nat. Protocols* **1** 1–38
- [15] Murakawa K, Kobayashi M, Nakamura O and Kawata S 1999 *IEEE Eng. Med. Biol. Mag.* **18** 70–2
- [16] Palanker D, Vankov A, Huie P and Baccus S 2005 *J. Neural Eng.* **2** S105–20
- [17] Yang W, Khan W, Wu J and Li W 2019 *J. Micromech. Microeng.* **29** 043001
- [18] Shapiro M G, Homma K, Villarreal S, Richter C-P and Bezanilla F 2012 *Nat. Commun.* **3** 1–11
- [19] Carvalho-de-Souza J L, Treger J S, Dang B, Kent S B H, Pepperberg D R and Bezanilla F 2015 *Neuron* **86** 207–17
- [20] Jiang Y et al 2016 *Nat. Mater.* **15** 1023–2016
- [21] Deisseroth K 2011 *Nat. Methods* **8** 26–9
- [22] Mickle A D et al 2019 *Nature* **565** 361–5
- [23] Fenno L, Yizhar O and Deisseroth K 2011 *Annu. Rev. Neurosci.* **34** 389–412
- [24] Lanmüller H, Bijak M, Mayr W, Rafolt D, Sauermann S and Thoma H 1997 *Artif. Organs* **21** 210–2 (<https://pubmed.ncbi.nlm.nih.gov/9148707/>)
- [25] Murakawa K, Kobayashi M, Nakamura O and Kawata S 1999 *IEEE Eng. Med. Biol. Mag.* **18** 70–2
- [26] Gutruf P and Rogers J A 2018 *Curr. Opin. Neurobiol.* **50** 42–9
- [27] Jakešová M et al 2019 *Sci. Adv.* **5** eaav5265
- [28] Rand D et al 2018 *Adv. Mater.* **30** 1707292
- [29] Silverå Ejneby M et al 2021 *Nat. Biomed. Eng.* **2021** 1–13
- [30] Hartmann F, Jakešová M, Mao G, Nikić M, Kaltenbrunner M, Derek V and Głowacki E D 2021 *Adv. Electron. Mater.* **7** 2001236
- [31] Głowacki E D, Tangorra R R, Coskun H, Farka D, Operamolla A, Kanbur Y, Milano F, Giotta L, Farinola G M and Sariciftci N S 2015 *J. Mater. Chem. C* **3** 6554–64
- [32] Derek V, Głowacki E D, Bednorz M, Demchyshyn S, Sariciftci N S and Ivanda M 2016 *Silicon Photonics and Photonic Integrated Circuits V (Proceedings of SPIE—the International Society for Optical Engineering 9891)* ed L Vivien et al (Bellingham, Washington: SPIE) (<https://doi.org/10.1117/12.2234980>)
- [33] Rola K P and Zubel I 2012 *Microsyst. Technol.* **19** 635–43
- [34] Moni P, Al-Obeidi A and Gleason K K 2017 *Beilstein J. Nanotechnol.* **8** 723
- [35] Martin P M 2009 *Handbook of Deposition Technologies for Films and Coatings* (Norwich, NY.: William Andrew; Oxford: Elsevier Science)
- [36] Sajjad M T, Ruseckas A and Samuel I D W 2020 *Matter* **3** 341–54
- [37] Merrill D R, Bikson M and Jefferys J G R 2005 *J. Neurosci. Methods* **141** 171–98